A&A 377, 428–441 (2001)
DOI: 10.1051/0004-6361:20011134

Astronomy & Astrophysics

The cluster of galaxies Abell 970⋆

L. Sodré Jr.[1], D. Proust[2], H. V. Capelato[3], G. B. Lima Neto[4], H. Cuevas[5], H. Quintana[6], and P. Fouqué[7]

[1] Departamento de Astronomia do IAG/USP, Av. Miguel Stefano 4200, 04301-904 São Paulo, Brazil
[2] Observatoire de Paris - Section de Meudon, DAEC, 92195 Meudon Cedex, France
e-mail: Dominique.Proust@obspm.fr
[3] Divisão de Astrofísica INPE/MCT, 12225-010 São José dos Campos, Brazil
e-mail: hugo@das.inpe.br
[4] Departamento de Astronomia do IAG/USP, Av. Miguel Stefano 4200, 04301-904 São Paulo, Brazil
e-mail: gastao@iagusp.usp.br
[5] Departamento de Física, Universidad de La Serena, Benavente 980, La Serena, Chile
e-mail: hcuevas@enterprise.dfuls.cl
[6] Departamento de Astronomia y Astrofísica, Pontificia Universidad Católica de Chile, Casilla 104, Santiago 22, Chile
e-mail: hquintan@astro.puc.cl
[7] European Southern Observatory, Casilla 19001, Santiago 19, Chile and
Observatoire de Paris – Section de Meudon, DESPA, 92195 Meudon Cedex, France
e-mail: pfouque@eso.org

Received 13 September 2000 / Accepted 14 June 2001

Abstract. We present a dynamical analysis of the galaxy cluster Abell 970 based on a new set of radial velocities measured at ESO, Pic du Midi and Haute-Provence observatories. Our analysis indicates that this cluster has a substructure and is out of dynamical equilibrium. This conclusion is also supported by differences in the positions of the peaks of the surface density distribution and X-ray emission, as well as by the evidence of a large-scale velocity gradient in the cluster. We also found a discrepancy between the masses inferred with the virial theorem and those inferred with the X-ray emission, which is expected if the galaxies and the gas inside the cluster are not in hydrostatic equilibrium. Abell 970 has a modest cooling flow, as is expected if it is out of equilibrium. We propose that cooling flows may have an intermittent behaviour, with phases of massive cooling flows being followed by phases without significant cooling flows after the accretion of a galaxy group massive enough to disrupt the dynamical equilibrium in the centre of the clusters. A massive cooling flow will be established again, after a new equilibrium is achieved.

Key words. galaxies: clusters: general – clusters: individual: A970 – distances and redshifts; large-scale structure of Universe; X-ray: general

1. Introduction

In the present accepted paradigm of structure formation, small structures are the first to collapse, then merging hierarchically to build larger objects. In this framework, clusters of galaxies, the largest (nearly) virialized structures, may be accreting galaxies and/or "dark haloes" even at $z = 0$ (e.g. Lanzoni et al. 2000). Therefore, the study of galaxy clusters may offer important informations for observational cosmology, because cluster properties depend on cosmological parameters and can be used to constrain cosmological scenarios. For instance, the cluster mass function, which may be described by the Press–Schechter formalism (Press & Schechter 1974), depends on the density parameter Ω_0 and on the power spectrum amplitude and shape parameter (e.g., Lacey & Cole 1994; Bahcall & Fan 1998). Also, the morphological and dynamical state of clusters allow us to infer their history and, again, to constrain cosmological theories of large-scale structure formation (e.g., Kauffmann et al. 1999).

Send offprint requests to: L. Sodré Jr.,
e-mail: laerte@iagusp.usp.br

⋆ Based on observations made at ESO, La Silla (Chile), Haute-Provence and Pic du Midi Observatories (France).

The mass of a cluster may be estimated by several methods: the optical virial mass, from the positions and radial velocities of the cluster galaxies; the X-ray mass, from the X-ray emission of the hot intracluster gas; the gravitational lensing mass, from the distortions produced on background object images by the gravitational field of the cluster. However, a discrepancy between these estimators are often found (e.g., Mushotzky et al. 1995; Girardi et al. 1998; Wu et al. 1998). Virial mass estimates rely on the assumption of dynamical equilibrium. X-ray mass estimates also depend on the dynamical equilibrium hypothesis and on the still not well-constrained intra-cluster gas temperature gradient (Irwing et al. 1999). Finally, mass estimates based on gravitational lensing are considered more reliable than the others (e.g., Mellier 1999) because they are completely independent of the dynamical status of the cluster, and their discrepancies with other methods may be due to non-equilibrium effects in the central region of the clusters (Allen 1998).

An important source of departure from equilibrium (that may affect mass estimates) are the substructures. Their very existence supports the current view that clusters grow hierarchically by accreting nearby groups and galaxies. Note that even the frequency and degree of clumpiness in the central regions of the clusters depends on the cosmology (e.g., Richstone et al. 1992). In many cases, substructures are loosely bound and can survive only a few crossing times in the hostile environment of rich clusters. However, they seem to be very common in present-day clusters. A recent estimate by Kolokotronis et al. (2000) indicates that at least 45% of rich clusters present optical substructures. Substructures are detected in both optical and X-ray images in 23% of the clusters. This last number may then be considered a lower limit on the fraction of real substructures in clusters, and it is large! Indeed, it implies that one in four clusters may be out of equilibrium due to the presence of a substructure. The dynamical status of individual clusters should therefore be examined in detail before being used in other studies.

In this paper we present a study of the dynamical status of the cluster Abell 970, from the analysis of the positions and velocities of cluster galaxies, as well as from the intra-cluster gas X-ray emission. Abell 970 has a richness class $R = 0$ and type B-M III (Abell et al. 1989). Together with a few other clusters (A979, A978 and A993), it is member of the Sextans supercluster (number 88 in the catalogue of Einasto et al. 1997; and number 378 in the catalogue of Kalinkov et al. 1998). It has a moderate cooling flow (White et al. 1997).

A search in the NED database[1] indicates that only 4 radial velocities are known in the field of the cluster (see Postman et al. 1992) which, however, have not been published. Here we examine some properties of the cluster Abell 970, using a set of 69 new radial velocities. The observations of radial velocities reported here are part of a program to study the dynamical structure of clusters of galaxies, started some years ago and with several results already published (see e.g. Proust et al. 1987, 1988, 1992, 1995, 2000; Capelato et al. 1991).

This paper is organized as follows. We present in Sect. 2 the details of the observations and data reduction. In Sects. 3 and 4 we discuss the galaxy and the X-ray distributions, respectively. In Sect. 5 we analyze the velocity distribution of the cluster galaxies. In Sect. 6 we present mass estimates for the central region of the cluster, derived from the optical and X-ray observations. In Sect. 7 we discuss the dynamical status of Abell 970. Finally, in Sect. 8 we summarize our conclusions. We adopt here, whenever necessary, $H_0 = 50\ h_{50}$ $\mathrm{km\,s^{-1}\,Mpc^{-1}}$, $\Omega_0 = 0.3$ and $\Omega_\Lambda = 0.7$.

2. Observations and data reductions

The new velocities presented in this paper have been obtained with the 1.52 m ESO telescope at La Silla (Chile), the 2.0 m telescope at Pic du Midi (France), and with the 1.93 m telescope at Haute-Provence Observatory (France).

Observations with the 1.52 m ESO telescope were carried out in February 1996. We used the Boller and Chivens spectrograph at the Cassegrain focus, equipped with a 600 lines/mm grating blazed at 5000 Å and coupled to an RCA CCD detector (1024×640 pixels) with a pixel size of 15 μm. The dispersion was 172 Å/mm, providing spectral coverage from 3750 to 5700 Å. The exposure times ranged between 30 and 60 min, according to the magnitude of the object. During the run, calibration exposures were made before and after each galaxy observation using an He-Ar source.

Observations with the 1.93 m Haute-Provence Observatory telescope were carried out in November 1997, November 1998 and April 2000. We used the CARELEC spectrograph at the Cassegrain focus, equipped with a 150 lines/mm grating blazed at 5000 Å and coupled to an EEV CCD detector (2048×1024 pixels) with a pixel size of 13.5 μm. The dispersion of 260 Å/mm allowed a spectral coverage from 3600 to 7300 Å. Wavelength calibration was done using exposures of Hg-Ne lamps.

Part of the velocities were obtained during an observing run at the 2.0 m Bernard Lyot telescope at Pic du Midi Observatory in January 1997. Despite the declination of Abell 970, we used the ISARD spectrograph in its long-slit mode with a dispersion of 233 Å/mm with the TEK chip (1024×1024 pixels) of 25 μm, corresponding to 5.8 Å/pixel. Typically, two exposures of 2700 s each were taken for fields across the cluster. Wavelength calibration was done using Hg-Ne lamps before and after each exposure.

[1] The NASA/IPAC Extragalactic Database (NED) is operated by the Jet Propulsion Laboratory, California Institute of Technology, under contract with the National Aeronautics and Space Administration.

Table 1. Heliocentric radial velocities for galaxies.

GALAXY	R.A (2000)	DEC. (2000)	TYPE	b_J^{cosmos}	VELOCITY $V \pm \Delta V$	R	N
01	10 17 25.7	–10 41 21	E/D	16.57	17 525 52	9.72	e
02	10 17 24.6	–10 41 22	S0	18.00	16 209 37	7.14	e
03	10 17 28.3	–10 40 59	S0/S	18.67	18 424 74	5.48	e
04	10 17 29.7	–10 40 31	S0	17.62	16 270 52	9.67	e
05	10 17 26.3	–10 41 34	S0	17.51	18 357 54	6.60	e
06	10 17 23.9	–10 42 16	S0/S	18.41	16 435 69	5.61	e
07	10 17 27.3	–10 41 51	E/S0	18.36	18 145 53	5.89	e
08	10 17 29.5	–10 42 17	S	18.38	17 404 71	7.42	e
09	10 17 21.7	–10 42 56	S	17.96	17 631 61	6.91	e
10	10 17 24.3	–10 43 29	S	17.95	16 341 81	6.76	e
11	10 17 31.8	–10 42 59	S0/S	18.83	17 769 81	5.79	e
12	10 17 30.0	–10 43 09	S0	18.45	17 327 35	5.57	e
13	10 17 32.9	–10 43 52	S	18.26	16 974 36	5.14	e
14	10 17 29.4	–10 44 34	Sa	17.69	18 909 75	5.61	e
15	10 17 28.0	–10 44 18	S0	17.67	18 030 29	8.46	e
16	10 17 20.7	–10 44 16	S	18.56	17 711 26	5.85	e
17	10 17 15.6	–10 43 28	Sa	17.51	19 503 96	2.62	e
18	10 17 12.9	–10 42 47	S0	17.83	19 450 51	9.10	e
19	10 17 35.6	–10 39 55	Sb	17.15	18 789 24	9.41	e
20	10 17 28.1	–10 39 27	Sa	18.16	16 842 76	4.79	e
21	10 17 27.6	–10 39 12	S0	18.63	16 404 92	4.48	e
22	10 17 21.0	–10 40 13	S0	17.18	18 788 45	9.41	e
23	10 17 23.2	–10 40 18	E	18.26	19 381 40	10.12	e
24	10 17 22.0	–10 39 45	E	18.00	16 847 47	6.37	e
25	10 17 22.5	–10 39 50	E/S0	17.09	19 483 54	9.32	e
26	10 17 25.2	–10 41 07	E	18.87	17 081 93	3.15	e
27	10 17 28.5	–10 41 13	E	17.52	33 586 98	2.84	e
28	10 17 21.9	–10 43 12	E/S0	18.71	17 764 64	5.17	e
29	10 17 14.4	–10 39 16	S	18.46	18 415 94	3.44	e
30	10 17 12.6	–10 40 05	E/S0	17.69	16 533 80	5.36	e
31	10 17 33.6	–10 38 46	SB	17.88	17 779 109	4.68	e
32	10 17 44.6	–10 39 14	S0/S	18.09	17 992 33	7.55	e
33	10 17 32.4	–10 34 27	S0	19.01	17 606 98	2.75	e
34	10 17 30.7	–10 36 24	S	17.43	16 722 134	3.55	e
35	10 17 41.6	–10 35 46	S0/S	17.63	21 637 37	8.62	e

Data reduction was carried out with IRAF[2] using the *longslit* package. The spectra were rebinned uniformly in log wavelength, with a scale of 1 Å/bin. Radial velocities were determined using the cross-correlation technique (Tonry & Davis 1979) implemented in the RVSAO package (Kurtz et al. 1991; Mink et al. 1995), with radial velocity standards obtained from observations of late-type stars and previously well-studied galaxies.

Table 1[3] lists positions and heliocentric velocities for 69 individual galaxies in the field of the cluster. The entries in the table are:

1. identification number;
2. right ascension (J2000);
3. declination (J2000);
4. morphological type determined from a visual inspection of the Palomar sky survey (POSS) images;
5. b_J magnitude from the COSMOS/UKST Southern Sky Object Catalogue;
6. heliocentric radial velocity with its error ($km\,s^{-1}$);
7. R-value derived from Tonry & Davis (1979);
8. telescope and notes- **e**: 1.52 m ESO telescope, **o**: 1.93 m OHP telescope; **p**: 2.0 m Pic du Midi telescope.

For the analysis in the next sections it is important to estimate the completeness level of the velocity sample as a function of the magnitude. To do that (and also to study the cluster galaxy projected distribution) we extracted from the ROE/NRL COSMOS UKST Southern Sky Object Catalogue, supplied by the Anglo-Australian Observatory (Yentis et al. 1992), a sample of galaxies in the direction of the cluster. An examination of Table 1 indicates that, with one exception, all velocities were measured in a region of $\sim 27' \times 22'$ (in RA and DEC,

[2] IRAF is distributed by the National Optical Astronomy Observatories, which are operated by the Association of Universities for Research in Astronomy, Inc., under cooperative agreement with the National Science Foundation.

[3] Table 1 is also available in electronic form at the CDS via anonymous ftp to `(130.79.128.5)` or via `http://cdsweb.u-strasbg.fr/cgi-bin/qcat?J/A+A/377/428`.

Table 1. continued.

GALAXY	R.A (2000)	DEC. (2000)	TYPE	b_J^{cosmos}	VELOCITY $V \pm \Delta V$	R	N
36	10 17 51.1	–10 35 00	E	17.29	16 661 62	4.42	e
37	10 17 36.9	–10 46 01	S	16.8 [7]	11 957 79	4.97	e
38	10 17 36.8	–10 46 05	S0/S	16.8 [7]	12 221 77	4.70	e1
39	10 16 55.8	–10 38 51	Sa	17.83	17 570 74	7.53	e
40	10 16 58.5	–10 38 07	S0/S	16.42	17 184 44	6.33	e
41	10 16 59.7	–10 37 39	E	18.62	17 873 59	6.44	e
42	10 17 00.6	–10 37 12	E	19.16	17 194 66	5.58	e
43	10 17 03.9	–10 37 38	E/S0	18.11	17 690 52	7.14	e
44	10 17 11.8	–10 36 07	E/S0	16.43	21 998 84	8.33	e2
45	10 16 57.5	–10 40 16	E	17.46	17 903 48	9.11	e
46	10 17 02.0	–10 39 59	E	19.10	18 843 98	4.53	e3
47	10 17 07.6	–10 45 46	S0	16.89	17202 86	15.72	e4
48	10 17 10.2	–10 46 26	E/S0	17.13	17 475 46	12.24	e5
49	10 16 49.9	–10 47 23	Sb	16.91	17 487 64	6.73	e
50	10 17 00.5	–10 47 17	Sa	17.38	21 166 107	3.77	e
51	10 16 54.1	–10 43 10	S0/S	18.45	17 257 85	4.71	e
52	10 16 53.2	–10 43 43	E	18.83	17 351 85	6.70	e
53	10 17 47.0	–10 45 19	S	19.14	16 771 138	2.96	p
54	10 18 18.0	–10 46 48	E/S0	15.95	11 579 63	8.04	p
55	10 18 15.6	–10 45 03	S0	17.69	12 056 81	3.26	p
56	10 17 51.6	–10 44 47	E	19.44	16 372 89	2.53	p
57	10 17 54.6	–10 43 47	S0	19.44	45 962 93	2.61	p
58	10 18 06.9	–10 42 43	S	19.13	51 814 76	2.41	p
59	10 18 04.0	–10 41 44	SBc	19.68	48 068 73	3.01	p
60	10 17 57.7	–10 33 48	S	18.52	16 228 44	4.53	p
61	10 18 13.0	–10 34 42	S	18.47	11 675 69	5.34	o6
62	10 16 55.2	–10 30 49	S	18.16	18 371 133	3.30	o
63	10 16 54.7	–10 33 22	S	17.86	17 737 75	4.47	o
64	10 16 36.9	–10 32 38	S0	17.58	17 982 82	5.62	o
65	10 16 51.9	–10 36 15	S	17.53	18 255 84	5.39	o
66	10 16 48.8	–10 39 10	S0	18.67	18 293 63	6.48	o
67	10 17 42.0	–10 45 49	E	18.60	12 101 114	3.22	o
68	10 16 37.3	–10 32 39	?	18.77	17 589 136	3.04	o
69	10 16 41.3	–10 52 38	S	17.37	17 649 42	8.74	o

Emission lines: **1**: [OIII], Hα, [SII] = 12 084 km s^{-1}; **2**: Hα = 22 087 km s^{-1}; **3**: Hα = 18 858 km s^{-1}; **4**: Hα = 17 234 km s^{-1}; **5**: Hα = 17 523 km s^{-1}; **6**: measured on Hβ, [OIII], Hα; **7**: estimated magnitude (see Sect. 4).

respectively), centered on the position of galaxy number 1 in Table 1, which assured a good level of completeness in the core of the cluster. Indeed, by comparing the velocity and the COSMOS catalogues we verify that, within this region, our velocity sample is ∼92% complete at $b_J^{cosmos} = 18$, ∼75% at $b_J^{cosmos} = 19$, and ∼51% at $b_J^{cosmos} = 19.75$.

3. Galaxy distribution

We present in Fig. 1 the distribution of galaxies in the direction of Abell 970, obtained from the COSMOS catalogue, for galaxies brighter than $b_J^{cosmos} < 19.75$ (235 objects). The plot is centered on an E/D galaxy (number 1 in Table 1) and has $45' \times 45'$ (i.e., about $4.6 \times 4.6\ h_{50}^{-1}$ Mpc). It is interesting to point out that, amongst the galaxies with known velocities, this is the second brightest cluster galaxy ($b_J^{cosmos} = 16.57$).

The adaptive kernel density map (Silverman 1986) corresponding to this sample is given in Fig. 2. This figure indicates that the galaxy distribution in the field of Abell 970 is approximately regular, with the projected density peaking at the position of the E/D galaxy. There is a substructure at NW, near galaxy number 40 in Table 1. This is the brightest cluster galaxy (considering only galaxies with known radial velocities); it is classified as S0/S and has magnitude $b_J^{cosmos} = 16.42$. This figure also indicates that the cluster radial extension may attain several Mpc.

It is worth noting that all features displayed in this map are significant. The significance regions are obtained through a bootstrap resampling procedure applied to the sample coordinate distribution. This allows the construction of a map of standard deviations of the projected density. By subtracting the projected density map from the standard deviation map (multiplied by a given number, say 3), we define the *significance regions* of the projected

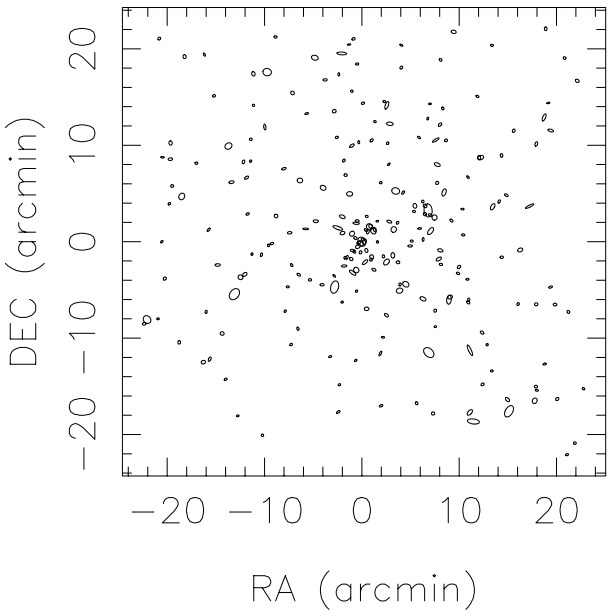

Fig. 1. Galaxies brighter than $b_{\rm J}^{\rm cosmos} = 19.75$ in the field of Abell 970. The plot is centered on galaxy number 1 in Table 1.

density map as those regions for which the resulting subtracted map is positive.

4. The X-ray emission and the gas distribution

Abell 970 is an X-ray source, first observed with *Einstein* IPC in June 1980 (Ulmer et al. 1981). It was also observed during the ROSAT all-sky survey (Voges 1992), in 1990, and is included in the X-ray Brightest Abell type Cluster catalogue (XBACs; Ebeling et al. 1996).

Some properties of the X-ray emission of Abell 970 were derived by White et al. (1997) from its *Einstein* IPC image. They applied a deprojection analysis that, to constrain the cluster gravitational potential, requires an X-ray temperature ($T_{\rm X}$) and velocity dispersion (σ) for the cluster. Due to the absence of temperature measurements for this cluster, these authors estimated it from a σ–$T_{\rm X}$ relation, assuming $\sigma = 832$ km s^{-1}. The result of the analysis is $T_{\rm X} = 4.1^{+0.2}_{-0.6}$ keV. Moreover, White et al. (1997), using this same data, suggests that Abell 970 has a weak cooling-flow, with a mass deposition rate $\dot{M} = 20^{+32}_{-20}\ M_\odot\,{\rm yr}^{-1}$ (see also Loken et al. 1999). Ebeling et al. (1996) determined the X-ray flux, luminosity and temperature using an iterative method running roughly as follows: assuming an initial X-ray temperature of 5 keV, the bolometric luminosity was computed. Then, with this luminosity and using the $T_{\rm X}$–$L_{\rm X}$ relation from White et al. (1997), a new estimate of the temperature was made which, in turn, was used to compute a new luminosity and so on. Thus, with ROSAT data and the above mentioned $T_{\rm X}$–$L_{\rm X}$ relation, Ebeling et al. (1996) quoted a flux equal to 9.9×10^{-12} erg cm^{-2} s^{-1}, luminosity of 1.50×10^{44} erg s^{-1} (both in the 0.1–2.4 keV band), and gas temperature $kT_{\rm X} = 3.6$ keV. By applying this same iterative method to the *Einstein* IPC data, Jones & Forman (1999) derived a X-ray luminosity of 2.13×10^{44} erg s^{-1} in the [0.5–4.5 keV] band and a bolometric luminosity equal to 3.79×10^{44} erg s^{-1}, corresponding to a temperature in agreement with the one given by Ebeling et al. (1996).

However, since the *Einstein* IPC detector has some spectroscopic capability, it is possible to estimate its temperature by a direct fitting of the available spectra. We have thus obtained both the "events" and image (in the 0.2–3.5 keV band, rebinned to 24 arcsec per pixel) files from the HEASARC Online Service. The spectrum of Abell 970 was extracted from the events file with XSELECT and analysed with XSPEC using the PI channels 4–12 (0.5–4.5 keV) within a region of 9.6 arcmin (corresponding to 1 h_{50}^{-1} Mpc). The X-ray emission was fitted with a single temperature, absorbed MEKAL model (Kaastra & Mewe 1993; Liedahl et al. 1995). We have also used the recipe given by Churazov et al. (1996) for computing the weights (available in XSPEC), based on the smoothed observed spectrum. With these weights, one can still use the least-square minimisation and the χ^2 statistics to estimate the confidence interval of the fitted parameters.

With only 9 bins covering the 0.5–4.5 keV band, it is impossible to constrain the metallicity. Therefore we have fixed Z to the "canonical" value of $\sim$0.3 $Z_\odot$, which is the mean value obtained for 40 nearby clusters by Fukazawa et al. (1998). Also, with only 3 bins with energy less than 1 keV, it is difficult to constrain independently the temperature and the hydrogen column density. This happens because they are anti-correlated (e.g. Pislar et al. 1997). Therefore, we have also fixed the hydrogen column density at $N_{\rm H} = 5.3 \times 10^{20}$ cm^{-2}, which is the galactic value at the Abell 970 position (Dickey & Lockman 1990). Figure 3 shows the fitting of the X-ray spectrum using the 9 available energy bins. The results are summarised in Table 2. The fitting shown in Fig. 3 presents large residuals at low energies ($\lesssim$1 keV), but beyond $\sim$2 keV, which is the region of the spectra most important for temperature determination, the residuals are acceptable. Nevertheless, it is worth stressing that the estimated temperature is strongly dependent on the number of energy bins employed in the analysis. For instance, keeping only the 8 bins with energy $\gtrsim$0.7 keV, the estimated temperature increases to $4.9^{+2.7}_{-2.1}$ kev, with $\chi^2/{\rm dof} = 11.6/6$, while with the 7 bins with energy larger than $\sim$1 keV the temperature is essentially unconstrained: $kT = 15.0^{+\infty}_{-12.2}$, with a $\chi^2/{\rm dof} = 4.2/5$.

The value of the gas temperature in Table 2, $kT = 3.3$ keV, is well below the IPC upper energy cutoff at 4.5 keV. Although slightly cooler, this value of temperature is in agreement with those derived by Ebeling et al. (1996) and White et al. (1997), because its error is large ($\sim$1 keV at the 68% confidence level; at the 90% confidence level our standard solution gives an upper limit for kT of 5.4 keV), due mainly to the small number

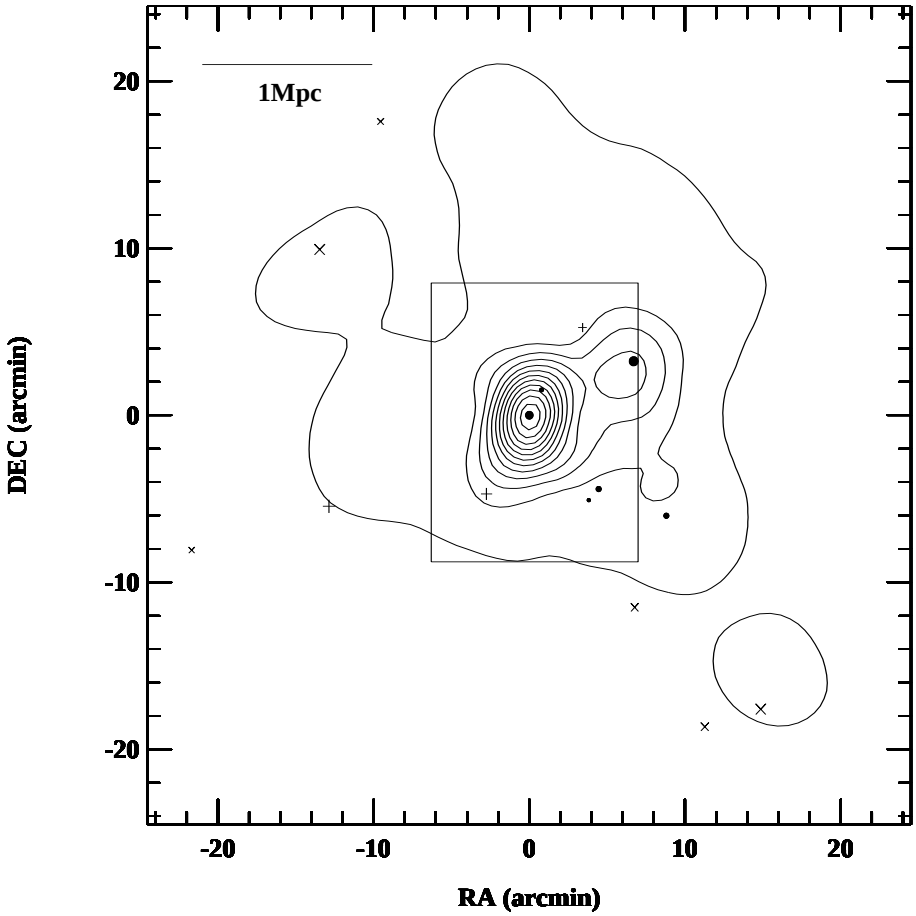

Fig. 2. Projected density map of the galaxies brighter than $b_{\rm J}^{\rm cosmos} = 19.75$ in the field of Abell 970, together with the positions of the 15 brightest ones. The peak density of this map corresponds to about 210 galaxies Mpc^{-2} h_{50}^2. All density levels in this map are significant. Other symbols are as follows- dots: galaxies kinematically linked to the cluster; pluses: galaxies projected in this field but not belonging to the cluster; crosses: galaxies with no measured velocities. The central rectangle displays the area covered by the X-ray image of Fig. 4. The substructure at NW, at ∼(7,3), is centered near galaxy number 40 of Table 1 (see text).

Table 2. X-ray spectral fitting results. kT is the gas temperature, $N_{\rm H}$ is the hydrogen column density, Z is the metallicity, $L_{\rm X}$ is the [0.5–4.5 keV] non-absorbed luminosity inside 1 h_{50}^{-1} Mpc, and the last column gives the χ^2 and number of degrees of freedom. Errors are at a confidence level of 68%.

kT (keV)	$N_{\rm H}$ (10^{20} cm^{-2})	Z ($Z_\odot$)	$L_{\rm X}$ (10^{44} ergs s^{-1})	χ^2/dof
$3.3^{+1.1}_{-0.7}$	5.3*	0.3*	$1.74^{+0.09}_{-0.10}$	18.1/7

Notes: *Fixed values. Varying the metallicity from 0.1 to 0.5 $Z_\odot$ produces a change in temperature of less than 0.3 keV, increasing towards $Z = 0.1$ $Z_\odot$.

of energy bins. We find no evidence from the data for systematic errors due to unusual background (e.g., solar flares). Using the $\sigma - T_{\rm X}$ relation given by Wu et al. (1999), the temperature in Table 2 corresponds to σ in the range 640–720 km s^{-1}.

In Fig. 4 we display the X-ray isophotes of an *Einstein* IPC image in the [0.2–3.5 keV] band. This image has 24 arcsec per pixel. As it can be seen, the X-ray isophotes are also regular but, interestingly, their peak is not coincident with the peak of the projected density distribution, being slightly displaced towards the NW substructure associated to the cluster brightest galaxy (see Fig. 2).

Figure 4 also suggests that there is no X-ray emission excess near this substructure. To verify whether this is indeed true, we have performed a wavelet multi-scale reconstruction on the IPC image. We have used the package MVM, "*Modèle de Vision Multi-Échelle*", described in detail by Rué & Bijaoui (1997; see also Slezak et al. 1994 for an application to X-ray cluster images). With this method, we can remove (spatial) high frequency noise while retaining small-scale genuine (with 3σ confidence level) objects. The wavelet image restoration technique is able to locate structures at various scales simultaneously and superposed objects may be revealed. The result of this analysis is also shown in Fig. 4. No emission excess is seen near the substructure. This is also consistent with the hypothesis that

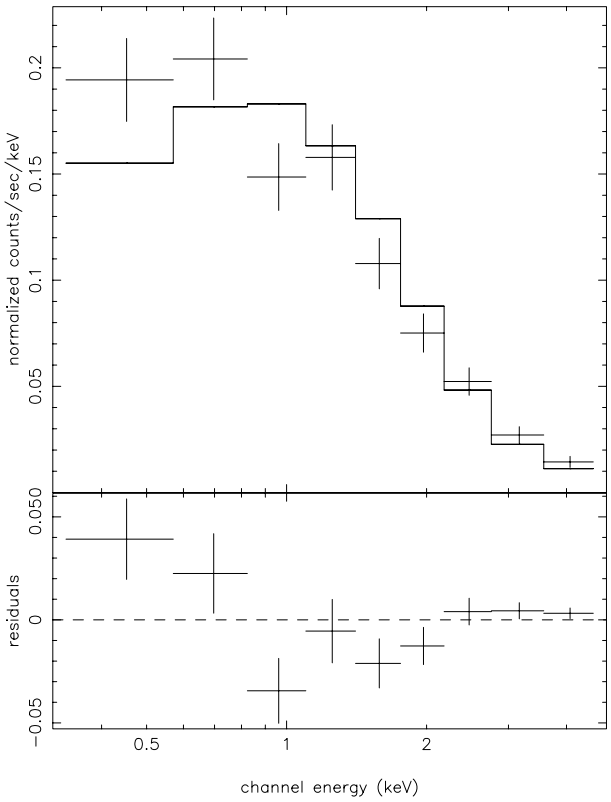

Fig. 3. Fit of the Abell 970 IPC X-ray spectrum. Both the metallicity and hydrogen column density are fixed (0.3 $Z_\odot$ and 5.3×10^{20} cm^{-2}, respectively).

the galaxies in this substructure are members of a group recently captured by the cluster, whose X-ray emission is much lower than that of the cluster.

Since the relaxation time of the hot gas is expected to be much lower than that of the galaxies, the non-coincidence between the peak of the galaxy distribution and the X-ray emission may be evidence of a state of non-equilibrium in the galaxy distribution, as expected if the substructure associated with the brightest galaxy has only recently fallen into the cluster. We will explore this point further in next sections.

The X-ray isophotes (even in the restored image) also show a small peak SE of the cluster centre, at the position of galaxies number 37 and 38 in Table 1, identified in the COSMOS catalogue as just one galaxy with magnitude $b_{\rm J}^{\rm cosmos} = 16.07$. However, an examination of the optical image of this object using POSS indicates that it indeed corresponds to two merging galaxies. A butterfly-shape due to the tidal currents induced by the merger can be noticed in the image and the spectrum of object number 38 has emission lines. It is somewhat surprising that this system is not catalogued as an IRAS source. The excess of X-ray emission associated with this galaxy pair may be evidence of an active nucleus excited by the merger. The magnitudes given in Table 1 were estimated from the COSMOS magnitude assuming that both galaxies have the same luminosity.

5. Velocity analysis

Our sample contains 69 velocities in the direction of Abell 970. Figure 5 shows a wedge velocity diagram in the direction of the cluster in right ascension (up) and declination (down), and indicates that most of the velocities are between 15 000 and 20 000 km s^{-1}. A histogram of the velocity distribution is displayed in Fig. 6. In this section we will discuss the velocity distribution, looking for non-equilibrium effects.

5.1. The velocity distribution

Since the usual recursive 3σ-clipping (Yahil & Vidal 1977) failed to simultaneously remove the low ($v \sim 12\,000$ km s^{-1}) and high velocity ($v \sim 22\,000$ km s^{-1}) tails of the distribution, we decided to analyse the radial velocity distribution of the cluster by constructing four different data samples to which we applied several statistical tests in order to assess the normality of their parent distributions. These samples are: A, comprising all galaxies within 11 500 km s^{-1} $< v <$ 22 000 km s^{-1}; B, which is identical to sample A except that the high- and low-velocity tails have been removed, thus covering the range 16 200 km s^{-1} $< v <$ 19 600 km s^{-1}; C, which is similar to sample B added with the high-velocity tail, that is 16 200 km s^{-1} $< v <$ 22 000 km s^{-1}; D, comprising only galaxies in the range 16 200 km s^{-1} $< v <$ 18 500 km s^{-1}: this sample has been considered in view of a significant gap in the data occurring at $v \sim 18\,500$ km s^{-1} (see below).

The analysis was made using the ROSTAT statistical package (Beers et al. 1990; Bird & Beers 1993), which proposes various statistical tests based on the empirical distributions of samples. We roughly distinguish 3 categories of normality tests among those included in the ROSTAT package. The first one contains the so-called *omnibus* tests, which try to quantify the overall deviation of the velocity distribution from a Gaussian, such as the Cramer von-Mises W^2 test, the Watson U^2 test and the Anderson-Darling A^2 test (see Beers et al. 1991, for references). The Kolmogorof-Smirnov (KS) test, which directly calculates the consistency of the observed distribution with a Gaussian, may also be included in this class of tests. The second group of tests are devised to measure the shape of the outskirts of the distribution, such as the kurtosis test (the B2 test) and its robust counterpart, the Tail Index (TI) test (see Bird & Beers 1993, for a discussion), or to test its tail population, such as the a and the W tests, which are most sensitive to the tail of the underlying populations and the u test, which is sensitive to contamination by extreme values (see Yahil & Vidal 1977, for a discussion on these tests). Finally, there are tests which measure the asymmetry of the distribution: the skewness test (B1 test) and its robust version, the Asymmetry Index (AI) test (Bird & Beers 1993). For each of these tests, ROSTAT computes its statistics as well as their associated probabilities p.

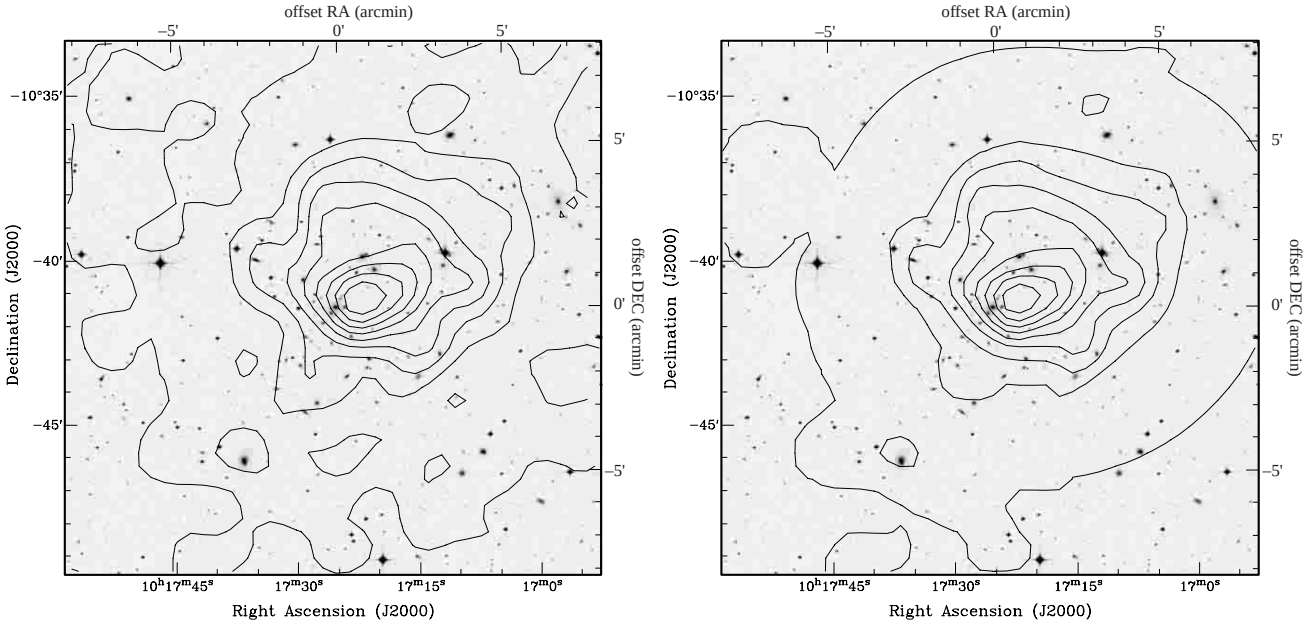

Fig. 4. Left: X-ray isophotes from an *Einstein* IPC image of Abell 970 (obtained from the HEASARC Online Service) superimposed on a DSS image of the cluster. Upper and left axes give the offset in arcmin from the galaxy number 1 in Table 1. The X-ray levels are linearly spaced. Right: same image but restored with wavelets (see text).

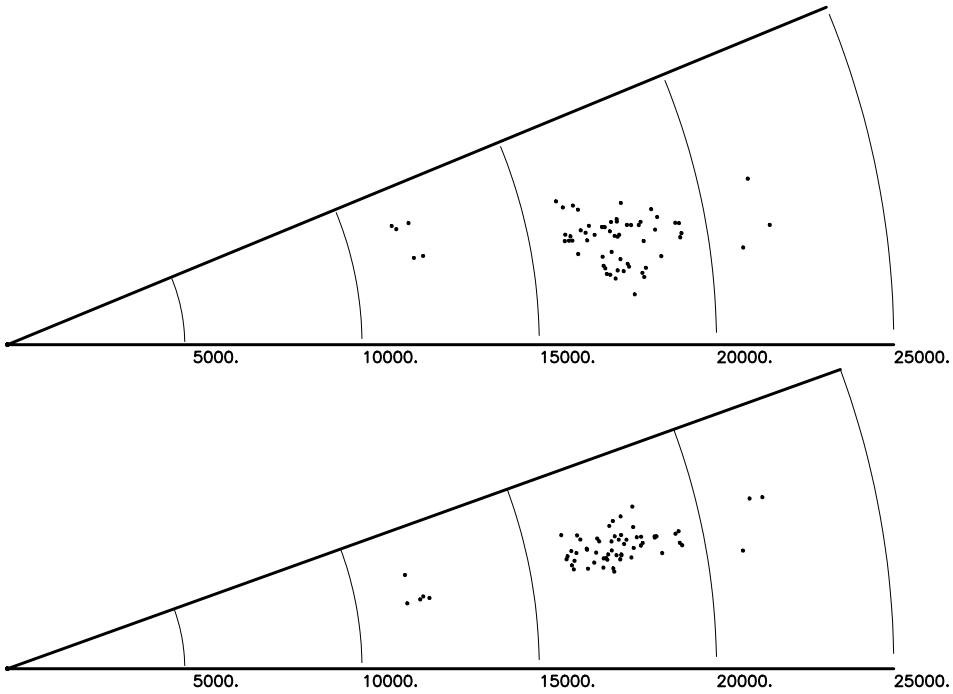

Fig. 5. Wedge velocity diagram in right ascension (up), and declination (down) for the measured galaxies in Abell 970 with radial velocities smaller than 25 000 $\mathrm{km\,s^{-1}}$.

The ROSTAT package also provides two statistical tests helping to identify kinematical substructures in the velocity distributions. These are the gap analysis (Wainer & Shacht 1978) and the Dip test unimodality (Hartigan & Hartigan 1985). The Dip test compares the observed distribution against an uniform one and as so is a conservative test for the unimodality of sample. The gap analysis estimates the probability that a gap of a given size and location, between the ordered velocities, may be produced by random sampling from a Gaussian population. A gap is considered significant if this probability is less than 0.03. As mentioned above, our radial velocity sample shows a significant gap at $v \sim 18\,500$ $\mathrm{km\,s^{-1}}$. This could be an indication that the distribution is bimodal. However, the Dip test failed to reject the unimodality at significance levels better than 10% for any of the samples.

In Table 3 we list, for each of the samples described above, the values of the statistics and the associated probabilities, p, for the tests discussed above. The B1 and B2 tests were discarded in favour of their robust versions, the AI and the TI tests. Moreover, because the results of the omnibus tests systematically agreed with the KS test, only the results for this last test have been quoted.

As can be seen from this Table, the normality hypothesis is rejected for samples A and C at significance levels better than 3% for all the statistical tests, except the u test. The values of the statistics of the a and W tests, as well as the TI values, indicate long-tailed underlying distributions, with sample C being significantly skewed towards high velocities, a consequence of removing the low-velocity tail from sample A. Removing both tails of sample A produces sample B, which seems nearly consistent with normality, as indicated by most of the tests. Although both the u and the W tests reject normality at high significance levels for this sample, their results seem contradictory, for the u statistics suggests a cutoff of the underlying distribution whereas the W statistics indicates it is long tailed. Notice that both the AI and TI tests are consistent with a normal underlying distribution for sample B. Very similar results were also obtained for sample D, but now the distribution seems slightly, but not significantly, skewed towards low velocities ($p(\mathrm{AI}) \sim 0.16$). This is not unexpected for, even if the marginal indication of bimodality of the distribution given by the gap analysis were confirmed, there would be no way, at this level of analysis, to disentangle galaxies belonging to one or to the other underlying distributions, that is, to B or D. Since the Dip statistics failed to reject unimodality for any of the samples, we will not consider this possibility for now, adopting sample B as representative of the radial velocity distribution of the cluster. We will return to this point at the end of this section.

We will thus assume that the cluster galaxies have radial velocities in the range between 16 200 and 19 600 km s^{-1}. It is interesting to note that a low-velocity tail at $v \sim 12\,000$ km s^{-1}, similar to the one found here, also affected the velocity distribution of the cluster Abell 979 (Proust et al. 1995), which is the nearest neighbour cluster of Abell 970 (at about 3° NE from its centre), both belonging to the same supercluster. This suggests the existence of a large foreground structure projected in this region of the sky.

Considering only the 56 galaxies within this velocity range, the cluster mean velocity is $\overline{V} = 17\,600 \pm 118$ km s^{-1} (corresponding to $z = 0.0587$)[4]. For comparison, the radial velocity of the E/D galaxy located at the centre of main cluster is $17\,525 \pm 52$, near that of the whole cluster, as should be expected if this is the dominant cluster galaxy. The cluster velocity dispersion, corrected following Danese et al. (1980) is $\sigma_{\mathrm{corr}} = 845^{+92}_{-69}$ km s^{-1} (at a confidence level of 68%). Figure 6 presents the radial velocity distribution of the cluster galaxies, as well as a Gaussian curve with the same mean velocity and dispersion observed for these galaxies. Note that this value of σ_{corr} is well above the value favoured by the $\sigma - T_{\mathrm{X}}$ relation, $\sim$700 km s^{-1} (cf. Sect. 4).

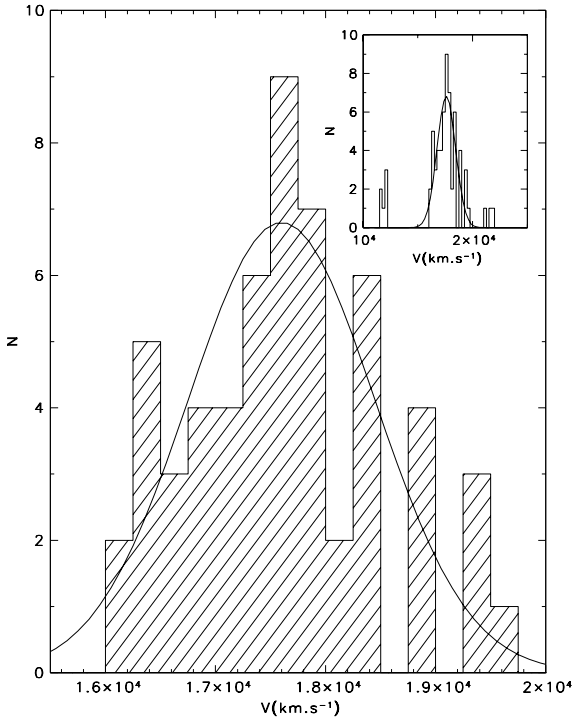

Fig. 6. The radial velocity distribution for the Abell 970 sample of galaxies. The continuous curve shows the Gaussian distribution corresponding to the mean velocity and velocity dispersion quoted in the text (normalized to the sample size and range). The inset displays the velocity distribution between 10 000 and 25 000 km s^{-1}.

If we consider the morphological types, the mean velocities and corrected velocity dispersions are: $\overline{V} = 17\,631$ km s^{-1} and $\sigma = 846^{+125}_{-87}$ km s^{-1} for E + S0 galaxies (35 objects), and $\overline{V} = 17\,655$ km s^{-1} and $\sigma = 841^{+185}_{-112}$ km s^{-1} for S + I galaxies (19 objects). Hence, contrary to what is observed in most clusters, where the velocity dispersion of the late type population tends to be larger than that of the early type population (Sodré et al. 1989; Stein 1997; Carlberg et al. 1997; Adami et al. 1998), in Abell 970 we do not see any significant difference between the velocity dispersion of these two populations. This might be another indication – besides the presence of a substructure – that Abell 970 is not in overall dynamical equilibrium.

5.2. Substructures in the galaxy distribution

Let us now consider again the substructure, as well as the peak of the galaxy distribution (cf. Fig. 2), taking into account the galaxy velocities. This analysis will be done with galaxies brighter than $b_{\mathrm{J}}^{\mathrm{cosmos}} = 19.0$, the magnitude where the completeness of our velocity catalogue in the central regions of the cluster is 75%.

[4] In this paper the mean and dispersion velocities are given as biweighted estimates, see Beers et al. (1990).

Table 3. Normality tests for the velocity distribution.

Sample	N	a	$p(a)$	u	$p(u)$	W	$p(W)$	p(KS)	AI	p(AI)	TI	p(TI)
(1)	(2)	(3)	(4)	(5)	(6)	(7)	(8)	(9)	(10)	(11)		
A	65	0.639	0.01	5.005		0.838	0.01	0.01	0.069		1.292	0.05
B	56	0.780		3.777	0.02	0.954	0.06		0.081		1.080	
C	59	0.711	0.01	4.730		0.881	0.01	0.01	1.057	0.04	1.273	0.05
D	48	0.829		3.403	0.01	0.940	0.02		–0.514		1.015	

We quote only those p values indicating a rejection of the null hypothesis at significance levels better than 10% (that is $p \leq 0.1$).

The substructure NW of the main cluster has, within a 3 arcmin (274 h_{50} kpc) circular region centered on the brightest S0/S galaxy, 7 cluster galaxies brighter than $b_{\rm J}^{\rm cosmos} = 19.0$. Together, these galaxies have a low velocity dispersion, $\sigma_{\rm NW} = 378^{+120}_{-77}$ km s^{-1}, more typical of that of loose groups. The mean velocity is $\overline{V}_{\rm NW} = 17\,834 \pm 135$ km s^{-1}, significantly higher than the overall mean velocity of the cluster. Our velocity catalogue contains 2 galaxies fainter that $b_{\rm J}^{\rm cosmos} = 19.0$ inside this region. Their inclusion does not significantly change the value of the mean velocity, although it increases the velocity dispersion to $\sigma_{\rm NW} = 525^{+160}_{-87}$ km s^{-1}, a value significantly lower than the cluster overall velocity dispersion. These results are consistent with the suggestion that this clump of galaxies forms a loose group infalling towards the cluster main central condensation. Arguing against the reality of such a group, we notice that its dominant S0/S galaxy is also the lowest velocity member, with $v = 17\,184$ km s^{-1}, but this is not statistically significant.

The central cluster condensation has a N-S elongation (see Fig. 2). A closer examination of the galaxy distribution indicates that this region is dominated by two small clumps of galaxies, which we will denote by A and B (see also Fig. 7 below). Considering circular regions of 1 arcmin ($\sim$91 kpc h$_{50}^{-1}$), the central clump, A, is tightly concentrated around the E/D galaxy, having 6 galaxies brighter than $b_{\rm J}^{\rm cosmos} = 19.0$ with $\overline{V_{\rm A}} = 17\,624$ km s^{-1}, and a dispersion $\sigma_{\rm A} = 816$ km s^{-1}. The other clump, B, is about 1.5 arcmin NW of clump A and is more sparse, with only 4 galaxies, of which 3 are tightly packed in velocity space with velocity dispersion $\sigma_{\rm B} = 711$ km s^{-1} and mean velocity $\overline{V}_{\rm B} = 19\,227$ km s^{-1}. The fourth galaxy that is, apparently, a member of this clump has, however, a very discrepant radial velocity, 16 847 km s^{-1}. Since it is not apparent in Fig. 2, it is not clear if B is a real substructure or a fortuitous projected group of cluster galaxies.

5.3. Velocity gradients

Figures 7 and 8 display, respectively, the adaptive kernel maps for the mean velocity and the mean velocity dispersion of the sample of cluster galaxies with measured radial velocities brighter than $b_{\rm J}^{\rm cosmos} = 18.9$. These maps were calculated from the local kernel weighted averages, with initial kernel size usually larger – in our case by a factor of 3, as a compromise between signal-to-noise and spatial resolution – than the optimal size prescribed by Silverman (1986), as suggested by Biviano et al. (1996). Significance regions for each map were obtained by a bootstrap, in a fashion similar to that applied to the projected density maps.

The mean velocity map of Fig. 7 clearly indicates the existence of a velocity gradient across the field, roughly in the E-W direction. This occurs because galaxies with $v > 18\,500$ km s^{-1} populate predominantly the East-side of the field. The mean velocity of the NW group discussed above is consistent with this gradient. Interestingly, this gradient is also consistent with the general gradient one would obtain by considering all galaxies of our catalogue with velocities between 12 000 and 22 000 km s^{-1}, suggesting that the cluster may be part of a larger structure running more or less in the E-W direction within, at least, this velocity range. In fact a (smaller) velocity gradient, in this same general direction, is also depicted by the mean redshifts of the supercluster members (cf. Einasto et al. 1997).

The mean velocity dispersion map displayed in Fig. 8 indicates that there is a radial gradient of the velocity dispersion. This was confirmed by direct calculations of the velocity dispersions within concentric regions centered in the E/D galaxy. Such a gradient is expected if the cluster grows through the capture of low velocity dispersion groups by the central, main galaxy concentration.

The above discussion points to the complexity of the velocity field of Abell 970. It is possible that the high velocity tail of the cluster velocity distribution displayed in Fig. 6 may be contaminated by another component with mean velocity $\overline{V} \gtrsim 18\,500$ km s^{-1}, which reveals itself trough the peculiarities of its spatial distribution. The fact that the velocity distribution shows some signs of bimodality, as pointed out at the beginning of this section, reinforces this suggestion. If real, this component could be interpreted as a diffuse halo located at the East-side of the cluster, probably infalling into its dark matter potential well. If correct, such a scenario may be revealed by some X-ray emission features typical of gas shocks produced during this infall.

6. Cluster mass

In this section we present mass estimates for Abell 970. We first consider the mass derived from its X-ray emission

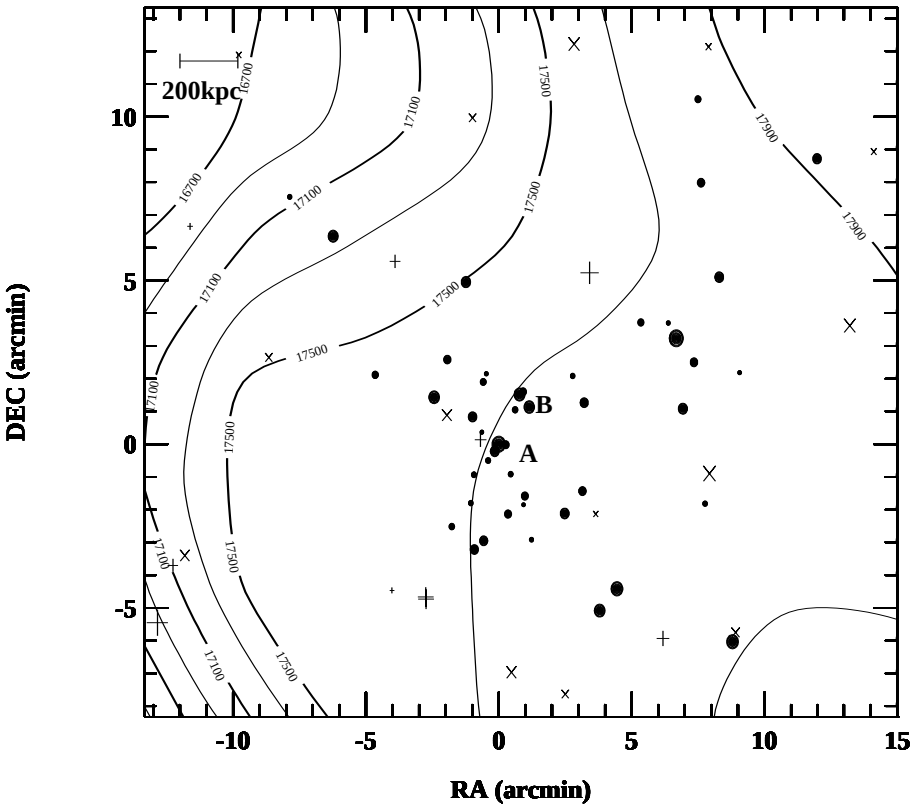

Fig. 7. Mean velocity map of the galaxies kinematically linked to the cluster and brighter than $b_{\rm J}^{\rm cosmos} = 18.9$. The positions of COSMOS galaxies brighter than this limit are also plotted, with symbols following Fig. 2. All regions of this map are significant. A and B correspond to the galaxy clumps discussed in Sect. 5.2.

and then we present masses computed from the velocity and galaxy distributions.

6.1. X-ray mass

Supposing that the gas is isothermal, in hydrostatic equilibrium and distributed with spherical symmetry, the dynamical mass inside r is given by:

$$M(r) = -\frac{k\,T_{\rm X}\,r}{G\,\mu\,m_{\rm p}}\frac{{\rm d}\log\rho(r)}{{\rm d}\log r}, \quad (1)$$

where μ is the mean molecular weight ($\mu = 0.59$ for a fully ionized primordial gas) and $m_{\rm p}$ is the proton mass. If we assume that the gas is described by a β-model,

$$\rho(r) = \rho_0(1 + (r/r_{\rm c})^2)^{-3\beta/2}, \quad (2)$$

the dynamical mass becomes:

$$M(r) = 6.68 \times 10^{10}\frac{\beta\,T_{\rm X}}{\mu}\frac{r^3}{r^2 + r_{\rm c}^2}\ M_\odot, \quad (3)$$

with r and $r_{\rm c}$ measured in kpc and $T_{\rm X}$ in keV.

Furthermore, if we have the density contrast $\delta = \bar{\rho}(r)/\rho_{\rm c}$ (where $\bar{\rho}(r)$ is the mean density inside the radius r and $\rho_{\rm c}$ is the critical density at the redshift of the cluster) then we can define r_δ as

$$\left(\frac{r_\delta}{r_{\rm c}}\right)^2 = \frac{2.3 \times 10^8}{\delta\,h_{50}^2\,f^2(z,\Omega_0,\Omega_\Lambda)}\frac{\beta\,T_{\rm X}}{\mu\,r_{\rm c}^2}, \quad (4)$$

where $f(z,\Omega_0,\Omega_\Lambda)$ depends on the cosmological parameters:

$$f^2(z,\Omega_0,\Omega_\Lambda) = \Omega_\Lambda + \Omega_0(1+z)^3 - (\Omega_0 + \Omega_\Lambda - 1)(1+z)^2. \quad (5)$$

When $\delta = 200$ we have the usual r_{200} radius, which is about the virial radius, $r_{\rm vir}$ (e.g. Lacey & Cole 1993).

The parameters of the β-model may be estimated from the fitting of the observed X-ray brightness profile, since $\Sigma_{\rm X} \propto 1/(1 + (R/r_{\rm c})^2)^{3\beta-1/2}$. The profile was obtained with the STSDAS/IRAF task *ellipse*; it extends only to $\sim$900 h_{50}^{-1} kpc. A least-squares fitting of this profile (see Fig. 9) gives: $\beta = 0.66 \pm 0.04$ and $r_{\rm c} = (260 \pm 20)\ h_{50}^{-1}$ kpc. The quality of the fitting is good: $\chi^2 = 8.4$ for 37 degrees of freedom. Taking $T_{\rm X} = 3.3$ keV (cf. Sect. 4), we obtain $r_{200} = 2.00^{+0.38}_{-0.28}$ Mpc and $M(r_{200}) = 4.8^{+1.5}_{-0.8} \times 10^{14}\ M_\odot$. The total mass in the region where the velocities have been measured is $M(r = 1200\,{\rm kpc}) = 2.79^{+1.18}_{-0.74} \times 10^{14}\ M_\odot$. White et al. (1997) obtained $M(r = 675$ kpc$) = 2.6 \times 10^{14}\ M_\odot$. This value is about 1.4 times larger than ours at the same radius (cf. Fig. 10 below), probably as a consequence of the high value of $T_{\rm X}$ assumed by these authors; anyway, within the errors both results are in agreement.

6.2. Optical virial mass

In Fig. 10 we show the cluster mass profile computed with the virial mass estimator (VME) which, as discussed by Aceves & Perea (1999), gives less biased mass estimates

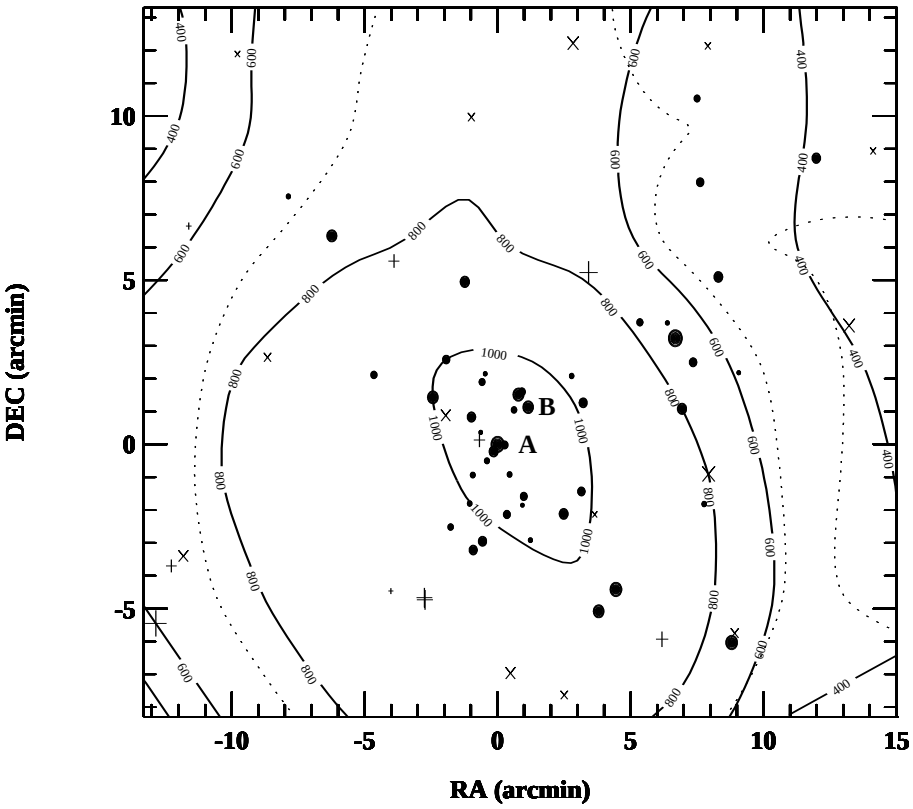

Fig. 8. Mean velocity dispersion map of the galaxies kinematically linked to the cluster and brighter than $b_{\rm J}^{\rm cosmos} = 18.9$. The positions of COSMOS galaxies brighter than this limit are also plotted, with symbols following Fig. 2. The dashed contours delineate the boundaries of the 99% significance levels regions of the map.

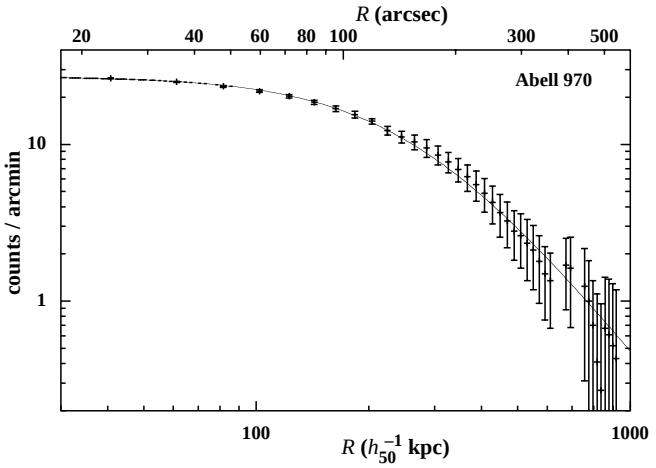

Fig. 9. X-ray brightness profile (IPC data with error bars), obtained with the STSDAS/IRAF task *ellipse*; the continuous line is the best-fit β-model.

when the system is not completely sampled. These authors also show that the VME overestimates the real mass by no more than 20% at small radii, being more reliable at larger apertures. The error bars in Fig. 10 are 1-σ standard deviations computed using the bootstrap method. The VME assumes, of course, that the system is virialized. In general, the presence of substructures or large-scale flows tend to increase the velocity dispersion of the galaxies, leading to an overestimation of the mass of the system.

The VME of Abell 970, within 1.2 h_{50}^{-1} Mpc, is $M = (6.80 \pm 1.34) \times 10^{14}\ M_{\odot}$, where the error, as before, was computed with the bootstrap method. Note that, for a virialized cluster, these are lower limits for the mass, since we have velocities only for the central region of the system. Indeed, assuming a relation between virial radius and velocity dispersion similar to that adopted by Girardi et al. (1998), we estimate that $r_{\rm vir} \sim 3.4\ h_{50}^{-1}$ Mpc, while the velocities have been measured within a region of radius $\sim$1.2 h_{50}^{-1} Mpc.

Figure 10 also displays the run of the total b_j luminosity of the cluster (up to $b_j = 19.75$). Considering the VME masses, we find that the mass-luminosity ratio ranges from 1360 $M_{\odot}/L_{\odot}$ at the cluster central region, to $\sim$450 $M_{\odot}/L_{\odot}$ at the largest aperture.

The mass profile derived from the X-ray emission is also presented in Fig. 10. The VME masses are in excess of the X-ray mass estimates by large factors, ranging from $\sim$16 for the central apertures, to about 4 at $\sim$1.3 h_{50}^{-1} Mpc aperture, which encompasses the whole velocity sample. These factors are well above the uncertainties discussed above for virialized clusters. In fact, the dynamical mass determined by the X-ray emission at radius $r \gg r_{\rm c}$ depends essentially on the temperature and the asymptotic slope of the gas density. Both are poorly determined with the available data; it is then possible that one of them

(or both) are under-estimated, which implies that we under-estimate the dynamical X-ray mass. For instance, if β is as high as 0.70 and $T_{\rm X} = 4.4$ (cf. the error bars in Table 2), then the dynamical X-ray mass would be twice the estimated value, i.e., $M(r = 1.2\ h_{50}^{-1}\ {\rm Mpc}) = 4.1 \times 10^{14}\ M_{\odot}$. On the other hand, the presence of a substructure associated with the cluster brightest galaxy, as well as the mean velocity gradient, may be an indication of non-virialization and, consequently, the VME may be largely overestimated.

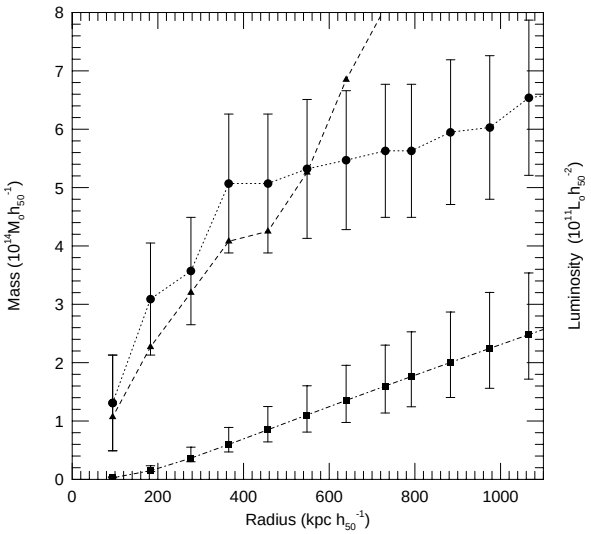

Fig. 10. Cluster optical masses (circles and dotted lines), X-ray masses (squares and dot-dashed lines) and luminosities (triangles and dashed lines).

7. The dynamical status of Abell 970

Several lines of evidence indicate that Abell 970 is not in an overall state of virialized equilibrium. Indeed, the presence of a substructure NW of the main galaxy concentration may indicate that the cluster has been capturing groups of galaxies in its neighbourhood. The large-scale gradient in the mean velocity of the galaxies, shown in Fig. 7, is also not expected in virialized systems. Other evidence for non-equilibrium include the discrepancy in the peaks of the X-ray emission and of the galaxy projected density, and the observed differences between optical and X-ray masses.

According to Allen (1998), there is a good agreement between X-ray and strong gravitational lensing mass measurements only in clusters with strong cooling flows; in clusters with modest or absent cooling flows, the masses determined from the X-ray data are 2 to 4 times smaller than those estimated from strong gravitational lensing. The reason for the mass discrepancy is the dynamical status of the central regions of the clusters: those with strong cooling flows are relaxed and virialized, while those with small cooling flows are out of equilibrium, and the assumption of hydrostatic equilibrium that underlies the X-ray mass estimates is not valid. Indeed, the presence or absence of cooling flows can be used as a diagnostic to verify whether galaxy clusters are in dynamical equilibrium in their central regions. Abell 970 has at most a weak cooling flow, of $\dot{M} = 20^{+32}_{-20}\ M_{\odot}\ {\rm yr}^{-1}$ (Ebeling et al. 1996), and our results, indicating that this system is not relaxed, are consistent with the findings of Allen (1998).

It is interesting to note that the offset between the X-ray and galaxy distribution centres, although significant, is not very large. It is possible that Abell 970 had a much stronger cooling flow until recently, that was interrupted by dynamical perturbations induced by the arrival of a galaxy group (now observed as a substructure) in the central regions of the cluster. Given that in the cluster densest regions the gas relaxes very quickly, compared with the time the galaxy distribution takes to achieve equilibrium, it is natural to think of cooling flows as an intermittent process that is disrupted by dynamical perturbations and that resumes activity after relaxation is achieved. The time scale of intermittence, in this scenario, depends strongly on the accretion rate of groups by the cluster.

8. Summary and conclusion

In this paper, we have presented an analysis of the galaxy cluster Abell 970, based on a new set of radial velocities and on X-ray observations. The study of the galaxy projected positions reveals a relatively regular distribution, centered on an E/D dominant galaxy. The analysis with the adaptive kernel density map indicates the presence of a statistically significant substructure NW of the cluster main galaxy concentration, centered on a S0/S galaxy that is the brightest cluster member. The X-ray emission distribution does not reveal any emission excess due to that substructure but, interestingly, the peak of the X-ray emission is not coincident with the cluster centre (at the position of the dominant galaxy), being displaced towards the direction of the substructure. These results suggest that this substructure is real and that the cluster may not be in an overall state of dynamical equilibrium.

Further evidence that the cluster is in a state of non-equilibrium comes from the analysis of the radial velocity distribution. For instance, the cluster velocity dispersion, 845 km s^{-1} (increasing to $\sim$1000 km s^{-1} at the cluster centre), is significantly larger than the value expected from the $\sigma - T_{\rm X}$ relation, that is, $\sim$700 km s^{-1}. Also, the substructure detected in the galaxy projected distribution has a much smaller velocity dispersion, 381 km s^{-1}, that is typical of loose groups. Together, these results suggest that this substructure may be a group that recently arrived in the central regions of the cluster. The presence of large scale velocity gradients is further evidence that Abell 970 is out of equilibrium. The virial mass of this cluster is much larger than the mass inferred from the X-ray emission. This discrepancy is indeed expected if the underlying hypothesis of these mass estimators, namely that galaxies

and gas inside the cluster are in hydrostatic equilibrium, is not actually fulfilled.

The fact that Abell 970 has a dim cooling flow also fits nicely in the above scenario if, as suggested by Allen (1998), only clusters in equilibrium exhibit massive cooling flows. Indeed, cooling flows may have an intermittent behaviour: phases of massive cooling flows may be followed by phases without significant cooling flows after the accretion of a galaxy group massive enough to disrupt the dynamical equilibrium in the centre of the clusters. After a new equilibrium is achieved, a massive cooling flow will be established again. Hence, in hierarchical scenarios for structure formation, intermittent cooling-flows should be a common phenomenon.

Acknowledgements. We thank the OHP, Pic du Midi and ESO staff for their assistance during the observations, and especially Gilles Charvin, student at the *École Normale Supérieure de Lyon* for his valuable scientific collaboration. We also thank Bill Forman and Christine Jones for valuable comments on the spectroscopic capability of the *Einstein* IPC detector, and Sergio Dos Santos for help with the wavelet package. LSJ, HVC, GBLN and HC thank the financial support provided by FAPESP, CNPq and PRONEX. DP and HQ acknowledge support from ECOS/CONICYT project C96U04. HQ was partly supported by the award of a Presidential Chair in Science (Chile). This research has made use of data obtained through the High Energy Astrophysics Science Archive Research Center Online Service, provided by the NASA/Goddard Space Flight Center, and of the ROE/NRL COSMOS UKST Southern Sky Object Catalog.

References

Abell, G. O., Corwin, H. G., & Olowin, R. P. 1989, ApJSS, 70, 1
Adami, C., Biviano, A., & Mazure, A. 1998, A&A, 331, 439
Allen, S. W. 1998, MNRAS, 296, 392
Aceves, H., & Perea, J. 1999, A&A, 345, 439
Bahcall, N. A., & Fan, X. 1998, ApJ, 504, 1
Biviano, A., Durret, F., Gerbal, D., et al. 1996, A&A, 311, 95
Beers, T. C., Flynn, K., & Gebhardt, K. 1990, AJ, 100, 32
Bird, C. M., & Beers, T. C. 1993, AJ, 105, 159
Capelato, H. V., Mazure, A., Proust, D., et al. 1991, A&AS, 90, 355
Carlberg, R. G., Yee, H. K. C., & Ellingson, E. 1997, ApJ, 478, 462
Churazov, E., Gilfanov, M., Forman, W., & Jones, C. 1996, ApJ, 471, 673
Danese, L., De Zotti, G., & di Tullio, G. 1980, A&A, 82, 322
Dickey, J. M., & Lockman, F. J. 1990, ARA&A, 28, 215
Ebeling, H., Voges, W., Bohringer, H., et al. 1996, MNRAS, 281, 799
Einasto, M., Tago, E., Jaaniste, J., Einasto, J., & Andernach, H. 1997, A&AS, 123, 119
Fukazawa, Y., Makishima, K., Tamura, T., et al. 1998, PASJ, 50, 187
Girardi, M., Giuricin, G., Mardirossian, F., Mezzetti, M., & Boschin, W. 1998, ApJ, 505, 74
Irwin, J. A., Bregman, J. N., & Evrard, A. E. 1999, ApJ, 519, 518
Jones, C., & Forman, W. 1999, ApJ, 511, 65
Kaastra, J. S., & Mewe, R. 1993, A&AS, 97, 443
Kalinkov, M., Valtchanov, I., & Kuneva, I. 1998, A&A, 331, 838
Kauffmann, G., Colberg, J. M., Diaferio, A., & White, S. D. M. 1999, MNRAS, 303, 188
Kolokotronis, V., Basilakos, S., Plionis, M., & Georgantopoulos, I. 2000, preprint [astro-ph/0002432]
Kurtz, M. J., Mink, D. J., Wyatt, W. F., et al. 1991, ASP Conf. Ser., 25, 432
Lacey, C., & Cole, S. 1993, MNRAS, 262, 627
Lacey, C., & Cole, S. 1994, MNRAS, 271, 676
Lanzoni, B, Mamon, G. A., & Guiderdoni, B. 2000, MNRAS, 312, 781
Liedahl, D. A., Osterheld, A. L., & Goldstein, W. H. 1995, ApJ, 438, L115
Loken, C., Melott, A. L., & Miller, C. J. 1999, ApJ, 520, L5
Mellier, Y. 1999, ARA&A, 37, 127
Mink, D. J., & Wyatt, W. F. 1995, ASP Conf. Ser., 77, 496
Mushotzky, R. F., Loewenstein, M., Arnaud, K., & Fukazawa, Y. 1995, in Dark Matter, ed. S. S. Holt, & C. L. Bennett (New York: AIP), 231
Postman, M., Huchra, J. P., & Geller, M. J. 1992, ApJ, 384, 404
Postman, M., & Lauer, T. R. 1995, ApJ, 440, 28
Press, W. H., & Schechter, P. 1974, ApJ, 187, 425
Proust, D., Talavera, A., Salvador-Solé, E., Mazure, A., & Capelato, H. V. 1987, A&AS, 67, 57
Proust, D., Mazure, A., Sodré, L., Capelato, H., & Lund, G. 1988, A&AS, 72, 415
Proust, D., Quintana, H., Mazure, A., et al. 1992, A&A, 258, 243
Proust, D., Mazure, A., Vanderriest, C., Sodré, L., & Capelato, H. V. 1995, A&AS, 114, 565
Proust, D., Cuevas, H., Capelato, H. V., et al. 2000, A&A, 355, 443
Richstone, D., Loeb, A., & Turner, E. L. 1992, ApJ, 393, 477
Rué, F., & Bijaoui, A. 1997, Exper. Astron., 7, 126
Slezak, E., Durret, F., & Gerbal, D. 1994, AJ, 108, 1996
Sodré, L., Capelato, H. V., Steiner, J. E., & Mazure, A. 1989, AJ, 97, 1279
Stein, P. 1997, A&A, 317, 670
Tonry, J., & Davis, M. 1979, AJ, 84, 1511
Ulmer, M. P., Kowalski, M. P., Cruddace, R. G., et al. 1981, ApJ, 243, 681
Voges, W. 1992, The ROSAT All-Sky X-ray Survey, in Proceedings of Satellites Symp. 3, ESA, ISY-3, 9
Wainer, H., & Shacht, S. 1978, Psichometrika, 43, 203
White, D. A., Jones, C., & Forman, W. 1997, MNRAS, 292, 419
Wu, X. P., Chiueh, T., Fang, L. Z., & Xue, Y. J. 1998, MNRAS, 301, 861
Wu, X. P., Xue, Y. J., & Fang, L. Z. 1999, ApJ, 524, 22
Yahil, A., & Vidal, N. V. 1977, ApJ, 214, 347
Yentis, D. J., Cruddace, R. G., Gursky, H., et al. 1992, in Digitized Optical Sky Surveys, ed. H. T. Gillivray, & E. B. Thomson (Kluwer Academic Pub., Dordrecht), 67